THE JOURNAL OF PHYSICAL CHEMISTRY A

Article

Cite This: J. Phys. Chem. A 2019, 123, 210−217

pubs.acs.org/JPCA

Combined Automated Reaction Pathway Searches and Sparse Modeling Analysis for Catalytic Properties of Lowest Energy Twins of Cu_{13}

Takeshi Iwasa,*[,†,‡,§] Takaaki Sato,[‡] Makito Takagi,[‡] Min Gao,[‡,§,∥] Andrey Lyalin,[⊥] Masato Kobayashi,[†,‡,§,#] Ken-ichi Shimizu,[§,∥] Satoshi Maeda,[†,‡,§,¶] and Tetsuya Taketsugu*[,†,‡,§,⊥,¶]

[†]Department of Chemistry, Faculty of Science, Hokkaido University, Sapporo 060-0810, Japan

[‡]Graduate School of Chemical Sciences and Engineering, Hokkaido University, Sapporo 060-0810, Japan

[§]ESICB, Kyoto University, Kyoto 615-8245, Japan

[∥]Institute for Catalysis, Hokkaido University, Sapporo 001-0021, Japan

[⊥]GREEN, National Institute for Materials Science, Tsukuba 305-0044, Japan

[#]PRESTO, Japan Science and Technology Agency, Kawaguchi 332-0012, Japan

[¶]Institute for Chemical Reaction Design and Discovery (WPI-ICReDD), Hokkaido University, Sapporo 001-0021, Japan

Supporting Information

ABSTRACT: In nanocatalysis, growing attention has recently been given to investigation of energetically low-lying structural isomers of atomic clusters, because some isomers can demonstrate better catalytic activity than the most stable structures. In this study, we present a comparative investigation of catalytic activity for NO dissociation of a pair of the energetically degenerated isomers of Cu_{13} cluster having C_2 and C_s symmetries. It is shown that although these isomers have similar structural, electronic, and optical properties, they can possess very different catalytic activities. The effect of isomerization between cluster isomers is considered using state-of-the-art automated reaction pathway search techniques such as an artificial force induced reaction (AFIR) method as a part of a global reaction route mapping (GRRM) strategy. This method allows effectively to locate a large number of possible reaction pathways and transition states (TSs). In total, 12 TSs for NO dissociation were obtained for Cu_{13}, of C_2, C_s, as well as I_h isomers. Sparse modeling analysis shows that LUMO is strongly negatively correlated with total energy of TSs. For most TSs, LUMO has the antibonding character of NO, consisting of the interaction between π^* of NO and SOMO of Cu_{13}. Therefore, an increase in the strength of interaction between NO molecule and Cu_{13} cluster causes the rise in energy of the LUMO, resulting in lowering of the TS energy for NO dissociation. The combination of the automated reaction pathway search technique and sparse modeling represents a powerful tool for analysis and prediction of the physicochemical properties of atomic clusters, especially in the regime of structural fluxionality, where traditional methods based on random geometry search analyses are difficult.

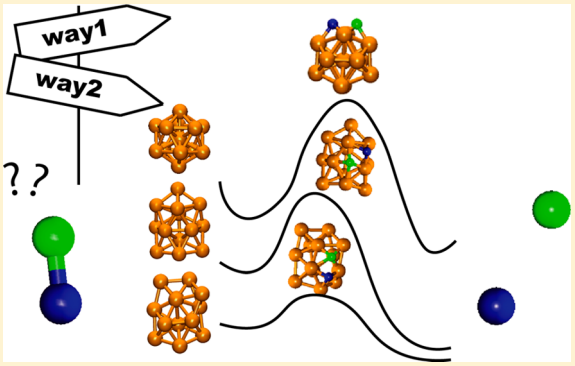

1. INTRODUCTION

Clusters consisting of up to several hundred atoms are known to possess nonscalable physicochemical and catalytic properties that are strongly dependent on size and composition; this is of interest in the search for new materials for optoelectronic devices, sensors, and catalysts.[1,2] Metals are known to possess catalytic properties through adsorption and exchange of electrons between small gas molecules and a variety of organic molecules; this is also true for noble or coinage metals known to be very inert in their bulk counterparts. Thus, for example, gold is known to catalyze CO oxidation at the nanometer scale,[3,4] leading researchers to explore its possible use in nanocatalysts.[5] The advantage of nanoclusters for catalysis is their potential to tailor the desired properties through appropriate choice of the number of atoms. With this ability, one can design new catalysts using abundant elements such as Cu, Fe, and Ni, instead of precious metals such as Pt, Pd, or Rh, with the latter being most widely used for three-way catalysis (TWC) in automobile exhausts.

Received: September 11, 2018
Revised: November 19, 2018
Published: December 12, 2018

DOI: 10.1021/acs.jpca.8b08868
J. Phys. Chem. A 2019, 123, 210−217

Theoretical studies have been indispensable in advancing understanding and design of novel cluster-based materials. Conventionally, a theoretical study of clusters begins by searching for the lowest energy structure for a given composition, followed by an investigation of physical and chemical properties. Many global structural searching methods e.g., the basin-hopping (BH) method[6,7] or genetic algorithms,[8,9] have been developed and utilized for global optimization, allowing identification of new most stable clusters for pure and multicomponent systems.[10−14] In contrast, recent theoretical studies have shown the importance of metastable low-energy isomers, in addition to the lowest energy isomer, by showing that the latter is not necessarily the best catalyst and low-energy isomers may have lower activation barriers.[15,16] Isomerization among low-energy isomers for clusters has also recently been discussed.[17] Although systematic reaction pathway searches are ideal for lowest energy isomers, computational complexity and costs have long represented significant constraints. With the advent of automated reaction pathway search methods,[18−20] we can better explore cluster catalysis, including low energy isomers and isomerization among them.[21−24]

In this study, we present a case study of Cu_{13}, using an artificial force induced reaction (AFIR) method[18−20] as part of a global reaction route mapping (GRRM) strategy[18,25] to overcome some of the above-mentioned difficulties, by efficiently locating reaction pathways and therefore transition states (TSs). Catalytic properties of pure and doped Cu clusters have recently been studied in industrially important catalysis fields, such as TWC for automobile exhaust conversions or methanol synthesis;[26−31] some of these studies have shown that Cu is one abundant element with possible catalytic properties for NO dissociation.[26,29,30] NO dissociation is said to be the most difficult, reaction-limiting step.[32,33] Precious metals are known to have best performance in TWC; however, they are expensive and rare and we therefore now need environmentally friendly and cost-effective alternatives, such as Cu. Experimental studies of nanocluster catalysts, combined with quantum chemical computations, improve our understanding and even the design of novel catalysts, while theoretical studies on Cu clusters have focused on lowest-energy isomers.[34−39] With regard to catalytic activity of Cu clusters/nanoparticles, recent theoretical studies have reported CO_2 reduction with Cu_{79}[31] or CO oxidation with Cu_{20}.[40]

This study focuses on Cu_{13} and the NO dissociation reaction to explore the potential application of the Cu_{13} cluster, utilizing automated reaction pathway searches. With this method, we can obtain many reaction pathways and related "big data". In recent years, informatics has begun to focus on handling large numbers of computational results in materials science.[41] In this study, we utilize sparse modeling for understanding complexity in the catalytic activity of fluxional clusters.

2. COMPUTATIONAL DETAILS

Density functional theory computations were performed mainly at the RI-B3LYP level[42−44] using the def-SV(P) basis sets,[45] as implemented in TURBOMOLE.[46,47] The B3LYP functional provides the best agreement with experimentally reported NO dissociation energies.[48] To obtain low energy isomers of Cu_{13}, we performed BH geometry searches,[6,7] starting from an icosahedral structure using the Atomic Simulation Environment (ASE)[49] with both BP86[50,51] and B3LYP functionals, with these giving similar results. Isomerization pathways of bare Cu_{13} clusters between lowest energy isomers were obtained using the single-component AFIR (SC-AFIR) method,[18−20] starting from C_2, C_s, and I_h structures with force parameter of γ = 3.109 eV (specified as 300 kJ/mol in an input file). All calculations gave the same lowest energy isomerization pathway. For isomerization from the I_h structure, the double-sphere AFIR (DS-AFIR) method[18,25] was also used. For searching dissociation pathways of NO with Cu_{13}, we utilized multicomponent AFIR (MC-AFIR) methods,[52,53] where Cu_{13}, N, and O are defined as separate fragments and artificial forces (AF) were set as positive between Cu_{13} and N or O, and negative between N and O, to dissociate N and O atoms, with an artificial force parameter of $\gamma \leq 6.219$ eV (600 kJ/mol). The terminate criterion NFault was set at 39 for NO dissociation pathway searches; the calculation finishes when already-obtained structures are found 39 times. This value corresponds to three times of the number of atoms, which was empirically suggested to obtain sufficient number of pathways.[25] A small number such as 3 is too small to confirm the presently obtained pathway/minima/TS are really good enough. All reaction pathway searches were performed utilizing a development version of the GRRM program.[18,54] In this program, geometries that are identical under the permutational symmetries (PS) are taken as the same equilibrium geometry. For example, a pathway connecting two geometries that are identical under the PS, is represented by $EQ_i - EQ_i$. Although not mentioned in eq 5 of ref 25., the number of isomers that are identical under the PS are counted in the Boltzmann distribution. To obtain isomerization pathways, network analysis was performed using the NetworkX library.[55] It should be noted that for reaction pathway searches, we use the Fermi smearing technique implemented in TURBOMOLE for determining electronic occupations without fixing the spin multiplicity. These pathways are refined with spin-fixed computations. However, the spin-consistent pathway was not found and therefore intersystem crossings were included in isomerization of the Cu_{13} cluster starting from I_h structure.

To extract key factors for the catalytic activity of Cu_{13} on NO dissociation, we performed sparse modeling analysis, namely, L1 regularized regression for 12 TSs of NO dissociation catalyzed by Cu_{13}. TS energy from the most stable NO adsorption structure was regressed with the descriptors listed in Table 1. These parameters include structural and electronic properties that are often used to analyze reactivity. Because the number of descriptors (N = 87) was larger than the number of sample TS structures (12), leading to an underdetermined system, the standard least-squares regression method could not be adopted. In the L1

Table 1. Descriptors Used in the L1 Regularized Regression of TS Energy for NO Dissociation on Cu_{13}

descriptor	no. of variables
HOMO energy [H] and LUMO energy [L]	2
dipole moment [D]	1
Mulliken charge [M(N, O, Cu1−13)]	15
natural charge [N(N, O, Cu1−13)]	15
NO distance [R_{NO}]	1
distance from N [R_N(Cu1−13)] and O [R_O(Cu1−13)]	26
Wiberg bond index for NO [W_{NO}]	1
Wiberg bond index for N−Cu [W_N(Cu1−13)] and O−Cu [W_O(Cu1−13)]	26

DOI: 10.1021/acs.jpca.8b08868
J. Phys. Chem. A 2019, 123, 210−217

regularized regression, as typified by the least absolute shrinkage and selection operator (LASSO),[56] descriptor selection and model construction (regression) were simultaneously performed by minimizing the following $l(\boldsymbol{\beta})$:

$$l(\boldsymbol{\beta}) = (\mathbf{y} - \boldsymbol{\beta}\mathbf{X})^{\mathrm{T}}(\mathbf{y} - \boldsymbol{\beta}\mathbf{X}) + \sum_{i=1}^{N} p(\beta_i) \tag{1}$$

where $\mathbf{y}$ represents the objective variable vector, with 12 TS energies in this case, $\mathbf{X}$ is the normalized descriptor matrix, and $\boldsymbol{\beta}$ is the regression coefficient vector. The last term of eq 1 is the penalty term allowing descriptor selection; in the LASSO case:

$$p^{\mathrm{LASSO}}(\beta_i) = \lambda|\beta_i| \tag{2}$$

λ is a regularization parameter, where larger λ leads to a smaller number of selected descriptors. We also adopted smoothly clipped absolute deviation (SCAD)[57] and MC_+[58] regressions, which adopt the following penalty terms:

$$p^{\mathrm{SCAD}}(\beta_i) = \begin{cases} \lambda|\beta_i| & \text{if } |\beta_i| \le \lambda \\ -(|\beta_i|^2 - 2\gamma\lambda|\beta_i| + \lambda^2)/2(\gamma - 1) & \text{if } \lambda < |\beta_i| \le \gamma\lambda \\ (\gamma + 1)\lambda^2/2 & \text{if } \gamma\lambda < |\beta_i| \end{cases} \tag{3}$$

$$p^{\mathrm{MC+}}(\beta_i) = \lambda \int_0^{|\beta_i|} \left\{1 - \frac{x}{\gamma\lambda}\right\}_+ \mathrm{d}x \tag{4}$$

respectively, to reduce the larger penalty of descriptors having an absolutely larger regression coefficient. The ncvreg package[59] in R software was used for LASSO, SCAD, and MC_+ regressions.

3. RESULTS AND DISCUSSION

First, we will show that the two lowest energy isomers are very similar in terms of geometric and electronic structures, as well as electronic and optical properties. We also show isomerization pathways for these isomers. We then show that even though these basic physicochemical properties are similar, catalytic activity for NO dissociation step can differ. It is important that we consider isomer effects in cluster catalysis studies, but this is difficult to do with theoretical methods that randomly sample low-energy structures, because it is necessary to trace trajectories for any structural changes in order to discuss chemistry. The power of automated reaction pathway searches will be demonstrated in this case. The complexity arising from fluxional metal clusters can also be overcome using statistical analysis.

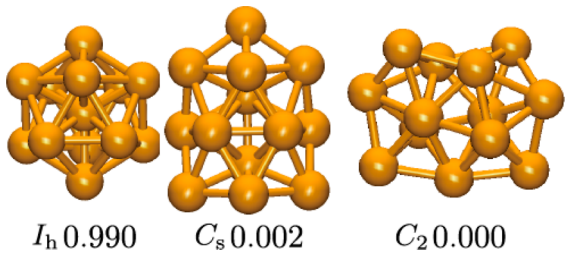

Figure 1. Optimized structures of Cu_{13}, together with molecular symmetry and relative energy in eV.

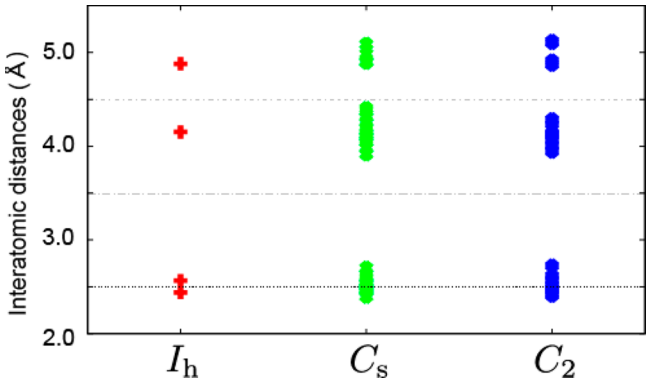

Figure 2. Interatomic distances of three isomers of Cu_{13}.

Table 3. HOMO−LUMO gap (HLG) energy, natural charge (Q), and dipole moment (d) of I_h, C_2, and C_s isomers obtained with B3LYP/def-SV(P)

	HLG (eV)	Q	d (Debye)
I_h	1.29	−0.172/0.014	0.00
C_s	1.03	−0.098 − 0.166	0.23
C_2	0.99	−0.078 − 0.130	0.33

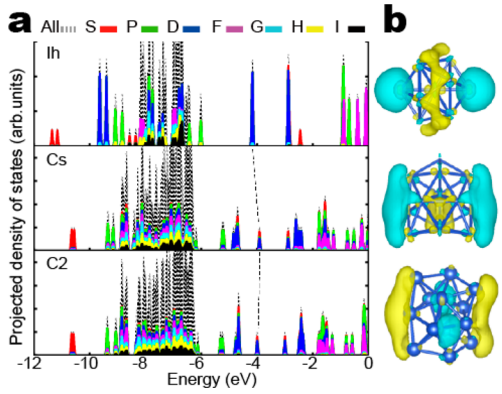

Figure 3. (a) Projected density of states for Cu_{13} of I_h, C_s, and C_2 isomers from top to bottom. Color labels are used to show weight of angular momentum for each KS orbital. The position of HOMO is indicated by the dotted line and (b) HOMO for these isomers. The positive and negative isosurfaces are shown by yellow and blue colors, respectively.

3.1. Lowest Energy Isomers of Cu_{13}. Figure 1 shows the optimized structures of Cu_{13} obtained by BH geometry optimizations. The I_h structure is the starting geometry of the BH optimization and the C_2 and C_s structures are the two

Table 2. Relative Total Energies in eV of I_h, C_2, and C_s Isomers for Different Computational Levels

	B3LYP/def-SV(P)	BP86/def-SV(P)	PBE/def-SV(P)	BP86/ecp-10-mhf
I_h	0.990	0.507	0.464	0.933
C_s	0.002	0.000	0.000	0.000
C_2	0.000	0.003	0.002	0.010

DOI: 10.1021/acs.jpca.8b08868
J. Phys. Chem. A 2019, 123, 210−217

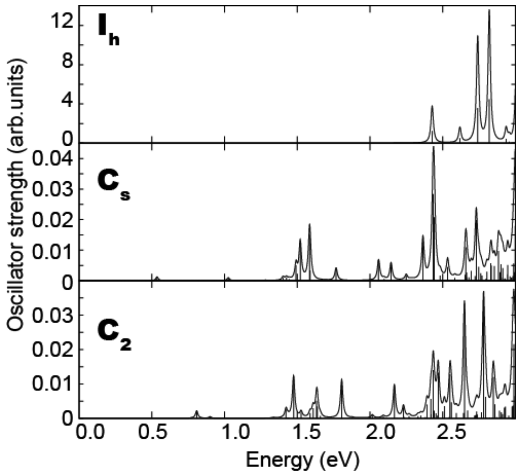

Figure 4. Simulated absorption spectra for Cu_{13} of I_h, C_s, and C_2 isomers (top to bottom). Line spectra are convoluted by a Lorentzian of width 0.05 eV.

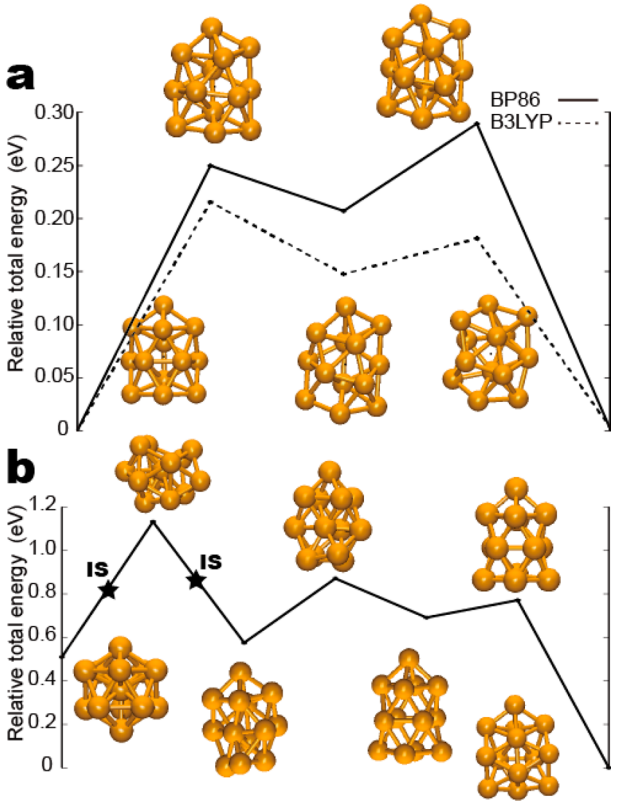

Figure 5. Isomerization pathway (a) from C_s to C_2 and (b) from I_h to C_s. Relative total energy in eV, compared to the lowest energy for each diagram. Solid and dashed lines are obtained with BP86 and B3LYP functionals, respectively. Molecules shown below and above the line are the equilibrium and transition state geometries, respectively. Stars indicate an intersystem crossing, i.e., with spin states changing along the pathway.

lowest energy isomers among many others. Table 2 summarizes relative total energies of these isomers obtained at the level of B3LYP, BP86, and PBE functionals along with def-SV(P) basis sets, and BP86 functional using 10-electron effective core potential. C_s and C_2 isomers are consistently energetically almost degenerate while the I_h isomer is about 0.5 to 1 eV higher in energy than these lowest energy isomers. The

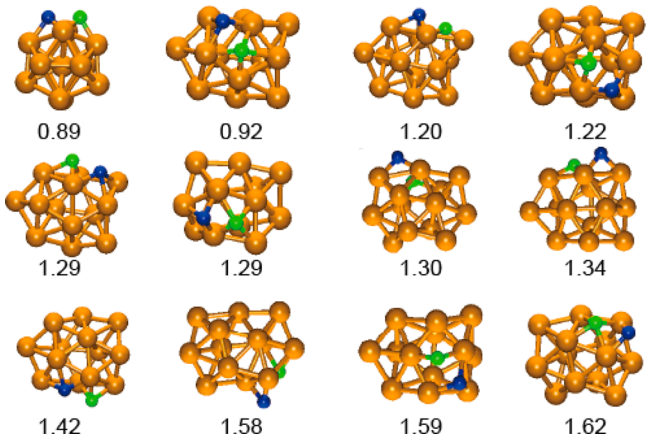

Figure 6. Transition states for NO dissociation at Cu_{13} in order of total energy (in eV). Relative total energy to the sum of the lowest Cu_{13} and NO (in eV) is shown, along with corresponding geometries. Blue, green, and gold spheres represent O, N, and Cu atoms, respectively.

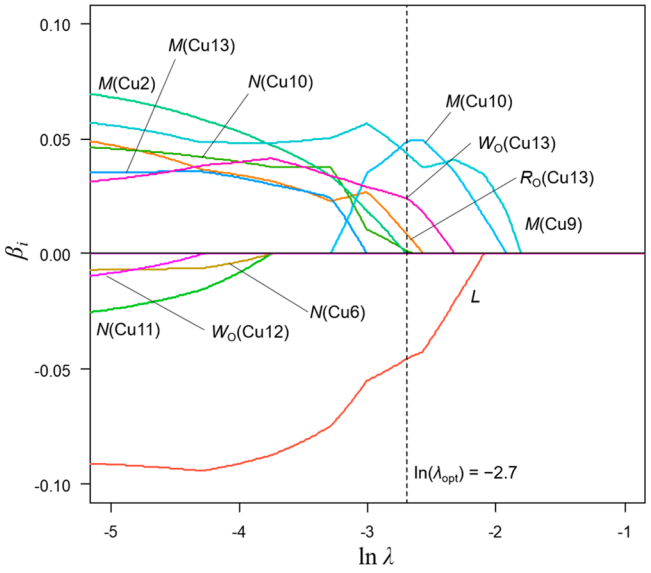

Figure 7. Dependence of LASSO regression coefficients for TS energies of NO dissociation on Cu_{13} cluster on the regularization parameter, λ. The cross validation score shows a minimum at $\ln(\lambda) = -2.7$, shown with a vertical dashed line. M, N, W_o, and R_o represent Mulliken charge, natural charge, Wiberg bond index, and distance from the O atom, respectively—see also Table 1.

Table 4. Selected Pearson Correlation Coefficients, *r*

descriptor	*r*
M(Cu9)	+0.725
M(Cu10)	+0.690
M(Cu13)	+0.618
L	−0.612
N(Cu10)	+0.584
W_O(Cu13)	+0.582
M(Cu4)	−0.547
M(Cu8)	+0.544

I_h isomer was once reported to be the lowest energy isomer for neutral Cu_{13}.[34] However, the later studies identified lower energy isomers than the I_h one.[35,36,38] The lowest energy isomers were found to have similar shapes to that reported in

DOI: 10.1021/acs.jpca.8b08868
J. Phys. Chem. A 2019, 123, 210−217

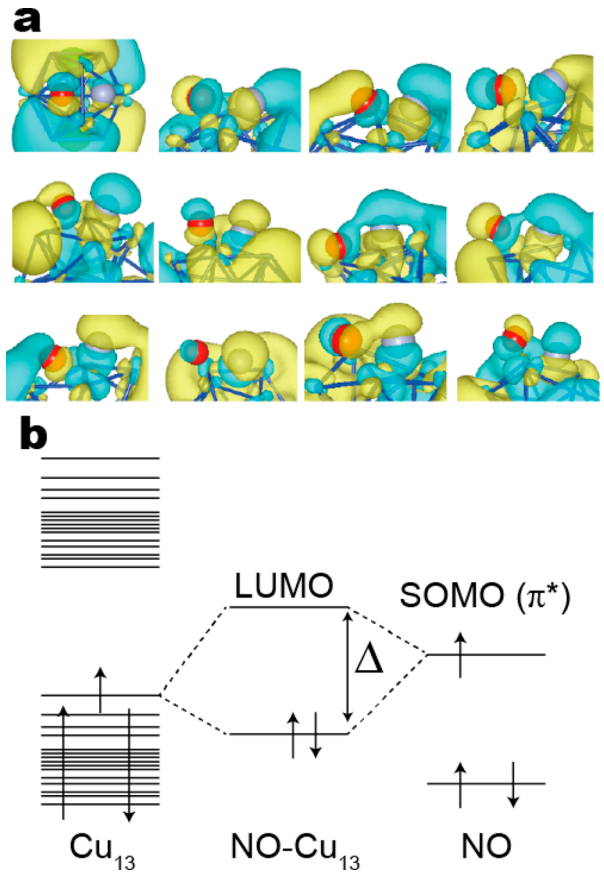

Figure 8. (a) LUMO for 12 TSs shown in Figure 6 in the same order. For atoms, color code of red O, gray N, blue Cu is used. The positive and negative isosurfaces of LUMO are shown by yellow and blue, respectively. (b) MO diagram for interaction between Cu_{13} and NO is schematically shown. Up and down spins are shown by arrows pointing upward and downward, respectively. Both the Cu_{13} and NO have singly occupied molecular orbital (SOMO) and the MO lower energies are fully occupied. For NO−Cu_{13}, the interaction between SOMOs of Cu_{13} and NO leads to energy splitting of Δ, which is large with stronger NO−Cu_{13} interaction.

previous studies,[36] while the energy difference in our case is smaller than reported in this study. The C_s isomer was previously reported as the lowest energy isomer of Cu_{13},[35,38] and together with C_2, these isomers are the energetically lowest. The use of different optimization techniques and/or different methods like functional, basis sets, and software leads to the different computational accuracy and convergence criteria. From these reasons, in the present study, we have checked several different functionals and basis sets, but all the methods give the same trend.

Figure 2 plots interatomic distances up to 5.5 Å. All clusters show similar distributions, with those of C_s and C_2 isomers broadened due to the lower molecular symmetry. Nearest neighbor Cu−Cu distances are about 2.5 Å. The I_h isomer has a core atom but all atoms in C_s and C_2 isomers are on the surface. Because of the high symmetry of the I_h isomer, unique adsorption sites are very limited and this is thus a good simple model. C_2 and C_s have a number of sites due to their lower symmetry.

3.2. Electronic and Optical Properties. Table 3 summarizes the HOMO−LUMO energy gap, natural charge, and dipole moment for these three isomers at B3LYP/def-SV(P). With regard to stable spin states, the I_h isomer is sextet and its HOMO is 5-hold symmetry h_g orbital, while C_2 and C_s isomers are doublet. Figure 3 shows the projected density of states (PDOS) onto the angular momenta of cluster and frontier orbitals. For PDOS, the Kohn−Sham (KS) orbitals for these clusters were projected onto spherical harmonics in a real-space grid. A capital letter is used to label the angular momentum of KS orbitals. S- and P-states (i.e., angular momentum of 0 and 1) are found below and above the 3d-band consisting of KS orbitals with angular momentum >6 because they have many nodes due to the localized nature of 3d atomic orbitals of Cu. HOMO of these clusters is mainly D_{z^2}. For lower-symmetry C_2 and C_s isomers, HOMOs mostly consist of D orbitals but are hybridized with S orbitals, thus having an S−D hybridized nature. The two lowest energy isomers appear to show very similar electronic structures.

Figure 4 shows simulated optical absorption spectra for I_h, C_s, and C_2 isomers. The I_h isomer has a small number of peaks compared to the others and no excited states are found around 0−2 eV. Although there are some minor differences, the two lowest energy isomers (C_s and C_2) show very similar structural and electronic properties, and behavior. For the I_h isomer, the peak around 2.5 eV is attributed to excitation from D (HOMO) to P, F states, while excited states with energy >2.5 eV are from P to S and from D to P, F states. For C_s and C_2 isomers, excited states up to 1.2 eV are interband transitions within S−D states around the Fermi level, while higher excited states are considered to be transitions from S−D to P−F hybridized states. The excited state characters of C_s and C_2 isomers are again very similar.

3.3. Isomerization. Figure 5 shows isomerization pathways between C_s and C_2 isomers and I_h and C_s isomers. This pathway is the minimum energy path obtained by SC-AFIR calculations using the BP86 functional. The total number of pathways between C_2 and C_s via intermediate states was 28,251, obtained from SC-AFIR calculations starting from I_h, C_2, and C_s isomers. The pathways consist of 12, 20, and 25 equilibrium structures, among obtained minima with total numbers of 36, 99, and 93, respectively, for these calculations. This minimum energy path was then updated using the B3LYP functional. Though the intermediate states obtained through IRC calculations with B3LYP starting from TSs were not exactly identical, their structural and energetic differences were marginal and can be considered negligible. As shown in Figure 5a, the pathways obtained with BP86 and B3LYP were similar, but the energy barrier was somewhat smaller with B3LYP. Although the two lowest energy isomers have almost the same energies and similar geometries, there is still an energy barrier of ∼0.3 eV with BP86 and ∼0.2 eV with B3LYP, suggesting that isomerization is likely to happen at room temperature. This result also indicates that, given the fraction of Cu_{13} in experimental synthesis, there would be at least two isomers with very similar electronic and optical properties, making it very difficult to distinguish between them.

It would be of interest to investigate changes in the appearance of the energy barrier from the high symmetry I_h structure to the lower symmetry isomers. Figure 5b shows an isomerization pathway from the I_h to the C_s isomer obtained with DS-AFIR using I_h and C_s isomers as fixed ends. It should be noted that the I_h isomer is sextet, while the TS next to the I_h is quartet. Other structures are doublet. These intersystem crossings are indicated by stars in the figure. The energy barrier from I_h to the next lower symmetry structure is about 0.6 eV,

DOI: 10.1021/acs.jpca.8b08868
J. Phys. Chem. A 2019, 123, 210−217

suggesting fast isomerization to the lower energy isomers, although this isomerization should be accompanied by intersystem crossings from higher to lower spin states. From an academic point of view, if the I_h isomer happens to form and immediately cool during the gas phase, this isomer could be isolated by, for instance, soft-landing to an inert surface such as graphite, under ultracold conditions.

3.4. Catalytic Activity for NO Dissociation and Sparse Modeling Analysis. Figure 6 shows the 12 TSs for NO dissociation pathways obtained by the automated reaction pathway search for C_2 and C_s isomers, as well as the manually obtained pathway for the I_h isomer, and the relative total energies to the sum of the lowest Cu_{13} and NO in eV. We first tried to correlate the energy ordering to physical values such as bond length, natural charges, or other structural and electronic properties, but this proved to be difficult. We therefore resorted to regression techniques to find physical values that are well correlated with these energy orderings. Energy diagram for these NO dissociation steps is shown in Figure S1 along with the structures for the lowest energy dissociation step for each Cu_{13} isomer. For these dissociation steps, the activation energies are 0.82, 1.25, and 0.51 eV for C_s, C_2, and I_h isomers, respectively. For estimating the activation barrier for NO dissociation, one should take the energy difference from the lowest energy molecular NO adsorption state and the lowest energy transition state. The estimated reaction barrier is 1.70 eV. This activation energy is somewhat lower compared to the Cu(111) case (1.9 eV),[60] perhaps due to the structural fluxionality of small clusters, i.e., the geometry change in the Cu_{13} cluster can be relaxed upon adsorption, lowering the energy of TSs, while Cu(111) is likely more rigid. The energy seems to be still larger than that of Rh(111) (1.25 eV),[61] notwithstanding different computational levels. In gas-surface reactions with bulk metal surface, nonadiabatic effects can be important owing to the continuous electronic states of metal.[62−64] However, in the present case, as shown in Figure 4, the lowest excited state energies of Cu_{13} are larger than 0.5 eV and therefore the nonadiabatic effects would not become dominant contributions compared to metal surfaces.

Figure 7 shows the dependence of the regularization parameter (λ) of regression coefficients by LASSO for TS structure energies for NO dissociation on the Cu_{13} cluster. These values were suitable for modeling the TS structure energies, correlating well with the latter. The optimal λ value, λ_{opt}, where the leave-one-out cross validation (LOO−CV) score gives a minimum, is shown in the figure with a dashed line. Table 4 also gives Pearson correlation coefficients for several descriptors showing high correlation. Cu atoms are numbered in ascending order of N−Cu distance. It can be confirmed that the LUMO energy (L) shows a large negative correlation over the wide range of λ. The Mulliken charges of several Cu atoms show positive correlation, while it is interesting that a strong correlation can be seen not only for atoms near the adsorbed molecule but also for those away from it. For example, the descriptors for Cu_{13} (the 13th Cu atom in the order of distance from N), furthest away from the adsorbate N, also appear to probably relate to the entire cluster structure. Although the first-appearing descriptors in LASSO [M(Cu9) and M(Cu10)] show absolutely large Pearson coefficients, the LUMO energy (L) gives the largest negative contribution through a wide range of λ values. The correlations between calculated and predicted TS energies by LASSO, SCAD, and MC_+, as well as regression coefficients at the optimal λ, are given in Supporting Information (Figures S2−S4).

By plotting LUMOs of 12 TSs in Figure 8a, we found that most of these orbitals have a NO antibonding nature. Considering the molecular orbital diagram shown in Figure 8b, given that the interaction between the singly occupied molecular orbital (SOMO) of NO and the valence band of Cu_{13} cluster is strong, the bonding and antibonding orbital energy splitting is large. The bonding orbital is buried below the Cu_{13} valence-band orbitals, while LUMO can be between the band gap of Cu_{13}. The strong interaction between the Cu_{13} cluster and NO results in higher LUMO energy and also stabilizes the Cu_{13}−NO complex. This is the reason why LUMO energy is negatively well correlated with the total energy of Cu_{13}−NO TS structures. Our study showed that sparse modeling analysis can be utilized for interpretation of quantum chemical calculation results.

4. CONCLUDING REMARKS

The present study demonstrates high potential of the AFIR method for investigation of isomerization and catalytic properties of atomic clusters. It is shown that although two considered isomers of Cu_{13} possess similar structural, electronic, and optical properties they demonstrate very different catalytic activity. Our findings indicate the important role of the structural isomers in catalysis. The present study also demonstrates that the methods of sparse modeling analysis become a powerful tool to overcome the complexity arising from automated reaction pathway searches giving many TSs for cluster catalysts, which in general make it difficult to trace the correct descriptors of catalytic activity.

■ ASSOCIATED CONTENT

Supporting Information

The Supporting Information is available free of charge on the ACS Publications website at DOI: 10.1021/acs.jpca.8b08868.

Energy profiles and representative geometric structures of NO dissociation reaction pathways whose transition states are shown in Figure 6 and correlations between the calculated and predicted TS energies by LASSO, SCAD, and MC_+ (PDF)

■ AUTHOR INFORMATION

Corresponding Authors

*(T.I.) E-mail: tiwasa@sci.hokudai.ac.jp.
*(T.T.) E-mail: take@sci.hokudai.ac.jp.

ORCID

Takeshi Iwasa: 0000-0002-1611-7380
Andrey Lyalin: 0000-0001-6589-0006
Masato Kobayashi: 0000-0002-4001-3581
Ken-ichi Shimizu: 0000-0003-0501-0294
Satoshi Maeda: 0000-0001-8822-1147
Tetsuya Taketsugu: 0000-0002-1337-6694

Notes

The authors declare no competing financial interest.

■ ACKNOWLEDGMENTS

We are grateful for financial support from the programs of the Ministry of Education, Culture, Sports, Science, and Technology (MEXT, Japan) "Elements Strategy Initiative to Form Core Research Center" (since 2012) and "Priority Issue

DOI: 10.1021/acs.jpca.8b08868
J. Phys. Chem. A 2019, 123, 210−217

on Post-K computer" (Development of new fundamental technologies for high-efficiency energy creation, conversion/storage and use). T.I., A.L., and T.T. gratefully acknowledge the financial support of JSPS KAKENHI Grant Nos. 18H04496, 15K05387, and 16KT0047, respectively. M.T. was supported by the MEXT through the Program for Leading Graduate Schools (Hokkaido University "Ambitious Leader's Program"). M.K. was supported by JST for PRESTO (Grant Number JPMJPR15N3). Institute for Chemical Reaction Design and Discovery (ICReDD) was established by World Premier International Research Initiative (WPI), MEXT, Japan. The computations were partly performed at the Research Center for Computational Science, Okazaki, Japan.

REFERENCES

(1) Luo, Z.; Castleman, A. W.; Khanna, S. N. Reactivity of Metal Clusters. *Chem. Rev.* **2016**, *116*, 14456−14492.
(2) Liu, L.; Corma, A. Metal Catalysts for Heterogeneous Catalysis: From Single Atoms to Nanoclusters and Nanoparticles. *Chem. Rev.* **2018**, *118*, 4981−5079.
(3) Haruta, M. Gold Catalysts Prepared by Coprecipitation for Low-Temperature Oxidation of Hydrogen and of Carbon Monoxide. *J. Catal.* **1989**, *115*, 301−309.
(4) Haruta, M. Size- and Support-Dependency in the Catalysis of Gold. *Catal. Today* **1997**, *36*, 153−166.
(5) Heiz, U.; Bernhardt, T.; Landman, U. Nanocatalysis. *Nanoscience and Technology* **2007**, 1.
(6) Wales, D. J.; Doye, J. P. K. Global Optimization by Basin-Hopping and the Lowest Energy Structures of Lennard-Jones Clusters Containing up to 110 Atoms. *J. Phys. Chem. A* **1997**, *101*, 5111−5116.
(7) Wales, D. J.; Scheraga, H. A. Global Optimization of Clusters, Crystals, and Biomolecules. *Science (Washington, DC, U. S.)* **1999**, *285*, 1368−1372.
(8) Vilhelmsen, L. B.; Hammer, B. Systematic Study of Au 6 to Au 12 Gold Clusters on MgO(100) F Centers Using Density-Functional Theory. *Phys. Rev. Lett.* **2012**, *108*, 126101.
(9) Vilhelmsen, L. B.; Hammer, B. A Genetic Algorithm for First Principles Global Structure Optimization of Supported Nano Structures. *J. Chem. Phys.* **2014**, *141*, 044711.
(10) Jiang, D. E.; Walter, M. Au40: A Large Tetrahedral Magic Cluster. *Phys. Rev. B: Condens. Matter Mater. Phys.* **2011**, *84*, 38−41.
(11) Iwasa, T.; Nakajima, A. Geometric, Electronic, and Optical Properties of a Boron-Doped Aluminum Cluster of : A Density Functional Theory Study. *Chem. Phys. Lett.* **2013**, *582*, 100−104.
(12) Palagin, D.; Reuter, K. M. Si20H20 Aggregates: From Simple Building Blocks to Highly Magnetic Functionalized Materials. *ACS Nano* **2013**, *7*, 1763−1768.
(13) Palagin, D.; Teufl, T.; Reuter, K. Multidoping of Si Cages: High Spin States beyond the Single-Dopant Septet Limit. *J. Phys. Chem. C* **2013**, *117*, 16182−16186.
(14) Ouyang, R.; Xie, Y.; Jiang, D. E. Global Minimization of Gold Clusters by Combining Neural Network Potentials and the Basin-Hopping Method. *Nanoscale* **2015**, *7*, 14817−14821.
(15) Gao, M.; Lyalin, A.; Takagi, M.; Maeda, S.; Taketsugu, T. Reactivity of Gold Clusters in the Regime of Structural Fluxionality. *J. Phys. Chem. C* **2015**, *119*, 11120−11130.
(16) Sun, G.; Sautet, P. Metastable Structures in Cluster Catalysis from First-Principles: Structural Ensemble in Reaction Conditions and Metastability Triggered Reactivity. *J. Am. Chem. Soc.* **2018**, *140*, 2812−2820.
(17) Zhai, H.; Alexandrova, A. N. Local Fluxionality of Surface-Deposited Cluster Catalysts: The Case of Pt7on Al2O3. *J. Phys. Chem. Lett.* **2018**, *9*, 1696−1702.
(18) Maeda, S.; Ohno, K.; Morokuma, K. Systematic Exploration of the Mechanism of Chemical Reactions: The Global Reaction Route Mapping (GRRM) Strategy Using the ADDF and AFIR Methods. *Phys. Chem. Chem. Phys.* **2013**, *15*, 3683.
(19) Maeda, S.; Taketsugu, T.; Morokuma, K. Exploring Transition State Structures for Intramolecular Pathways by the Artificial Force Induced Reaction Method. *J. Comput. Chem.* **2014**, *35*, 166−173.
(20) Maeda, S.; Harabuchi, Y.; Takagi, M.; Taketsugu, T.; Morokuma, K. Artificial Force Induced Reaction (AFIR) Method for Exploring Quantum Chemical Potential Energy Surfaces. *Chem. Rec.* **2016**, *16*, 2232−2248.
(21) Gao, M.; Lyalin, A.; Maeda, S.; Taketsugu, T. Application of Automated Reaction Path Search Methods to a Systematic Search of Single-Bond Activation Pathways Catalyzed by Small Metal Clusters: A Case Study on H-H Activation by Gold. *J. Chem. Theory Comput.* **2014**, *10*, 1623−1630.
(22) Gao, M.; Horita, D.; Ono, Y.; Lyalin, A.; Maeda, S.; Taketsugu, T. Isomerization in Gold Clusters upon O_2 Adsorption. *J. Phys. Chem. C* **2017**, *121*, 2661−2668.
(23) Tsutsumi, T.; Ono, Y.; Arai, Z.; Taketsugu, T. A Visualization of the Intrinsic Reaction Coordinate and Global Reaction Route Map by Classical Multidimensional Scaling. *J. Chem. Theory Comput.* **2018**, *14*, 4263−4270.
(24) Tsutsumi, T.; Harabuchi, Y.; Ono, Y.; Maeda, S.; Taketsugu, T. Analyses of Trajectory On-the-Fly Based on the Global Reaction Route Map. *Phys. Chem. Chem. Phys.* **2018**, *20*, 1364−1372.
(25) Maeda, S.; Harabuchi, Y.; Takagi, M.; Saita, K.; Suzuki, K.; Ichino, T.; Sumiya, Y.; Sugiyama, K.; Ono, Y. Implementation and Performance of the Artificial Force Induced Reaction Method in the GRRM17 Program. *J. Comput. Chem.* **2018**, *39*, 233−250.
(26) Nagai, Y.; Dohmae, K.; Nishimura, Y. F.; Kato, H.; Hirata, H.; Takahashi, N. Operando XAFS Study of Catalytic NO Reduction over Cu/CeO2: The Effect of Copper-Ceria Interaction under Periodic Operation. *Phys. Chem. Chem. Phys.* **2013**, *15*, 8461−8465.
(27) Vajda, S.; White, M. G. Catalysis Applications of Size-Selected Cluster Deposition. *ACS Catal.* **2015**, *5*, 7152−7176.
(28) Yang, B.; Liu, C.; Halder, A.; Tyo, E. C.; Martinson, A. B. F.; Seifert, S.; Zapol, P.; Curtiss, L. A.; Vajda, S. Copper Cluster Size Effect in Methanol Synthesis from CO_2. *J. Phys. Chem. C* **2017**, *121*, 10406−10412.
(29) Takagi, N.; Ishimura, K.; Matsui, M.; Fukuda, R.; Ehara, M.; Sakaki, S. Core-Shell versus Other Structures in Binary $Cu_{38-N}M_N$ Nanoclusters (M = Ru, Rh, Pd, Ag, Os, Ir, Pt, and Au; N = 1, 2, and 6): Theoretical Insight into Determining Factors. *J. Phys. Chem. C* **2017**, *121*, 10514−10528.
(30) Fukuda, R.; Takagi, N.; Sakaki, S.; Ehara, M. Structures of Bimetallic Copper-Ruthenium Nanoparticles: Incoherent Interface and Surface Active Sites for Catalytic Nitric Oxide Dissociation. *J. Phys. Chem. C* **2017**, *121*, 300−307.
(31) Dong, H.; Li, Y.; Jiang, D. First-Principles Insight into Electrocatalytic Reduction of CO_2 to CH_4 on a Copper Nanoparticle. *J. Phys. Chem. C* **2018**, *122*, 11392−11398.
(32) Hammer, B. The NO+CO Reaction Catalyzed by Flat, Stepped, and Edged Pd Surfaces. *J. Catal.* **2001**, *199*, 171−176.
(33) Tian, K.; Tu, X. Y.; Dai, S. S. NO Dissociation Pathways on Rh(1 0 0), (1 1 0), and (1 1 1) Surfaces: A Comparative Density Functional Theory Study. *Surf. Sci.* **2007**, *601*, 3186−3195.
(34) Fernández, E.; Soler, J.; Garzón, I.; Balbás, L. Trends in the Structure and Bonding of Noble Metal Clusters. *Phys. Rev. B: Condens. Matter Mater. Phys.* **2004**, *70*, 165403.
(35) Gutsev, G. L.; Mochena, M. D.; Bauschlicher, C. W. Dissociative and Associative Attachment of OH to Iron Clusters. *Chem. Phys. Lett.* **2005**, *407*, 180−185.
(36) Itoh, M.; Kumar, V.; Adschiri, T.; Kawazoe, Y. Comprehensive Study of Sodium, Copper, and Silver Clusters over a Wide Range of Sizes 2 < or = N < or = 75. *J. Chem. Phys.* **2009**, *131*, 174510.
(37) Guzmán-Ramírez, G.; Aguilera-Granja, F.; Robles, J. DFT Study of the Fragmentation Channels and Electronic Properties of Cu n ν (N= ± 1,0,2; N = 3−13) Clusters. *Eur. Phys. J. D* **2010**, *57*, 335−342.
(38) Baishya, K.; Idrobo, J. C.; Öğüt, S.; Yang, M.; Jackson, K. a.; Jellinek, J. First-Principles Absorption Spectra of Cu_{n} (N = 2−20) Clusters. *Phys. Rev. B: Condens. Matter Mater. Phys.* **2011**, *83*, 245402.

DOI: 10.1021/acs.jpca.8b08868
J. Phys. Chem. A 2019, 123, 210−217

(39) Singh, R. K.; Iwasa, T.; Taketsugu, T. Insights into Geometries, Stabilities, Electronic Structures, Reactivity Descriptors, and Magnetic Properties of Bimetallic Ni m Cu n-m (m = 1, 2; n = 3−13) Clusters: Comparison with Pure Copper Clusters. *J. Comput. Chem.* **2018**, *39*, 1878.
(40) Ma, L.; Melander, M.; Laasonen, K.; Akola, J. CO Oxidation Catalyzed by Neutral and Anionic Cu20 Clusters: Relationship between Charge and Activity. *Phys. Chem. Chem. Phys.* **2015**, *17*, 7067−7076.
(41) Ghiringhelli, L. M.; Vybiral, J.; Levchenko, S. V.; Draxl, C.; Scheffler, M. Big Data of Materials Science: Critical Role of the Descriptor. *Phys. Rev. Lett.* **2015**, *114* (1−5), 105503.
(42) Eichkorn, K.; Weigend, F.; Treutler, O.; Ahlrichs, R. Auxiliary Basis Sets for Main Row Atoms and Transition Metals and Their Use to Approximate Coulomb Potentials. *Theor. Chem. Acc.* **1997**, *97*, 119−124.
(43) Lee, C.; Yang, W.; Parr, R. G. Development of the Colle-Salvetti Correlation-Energy Formula into a Functional of the Electron Density. *Phys. Rev. B: Condens. Matter Mater. Phys.* **1988**, *37*, 785−789.
(44) Becke, A. D. Density-Functional Thermochemistry. III. The Role of Exact Exchange. *J. Chem. Phys.* **1993**, *98*, 5648−5652.
(45) Schäfer, A.; Horn, H.; Ahlrichs, R. Fully Optimized Contracted Gaussian Basis Sets for Atoms Li to Kr. *J. Chem. Phys.* **1992**, *97*, 2571−2577.
(46) *TURBOMOLE V6.4−7.3 2012−2018*; A Development of University of Karlsruhe and Forschungszentrum Karlsruhe GmbH, 1989−2007, TURBOMOLE GmbH, since 2007; Available from http://www.turbomole.com.
(47) Ahlrichs, R.; Bär, M.; Häser, M.; Horn, H.; Kölmel, C. Electronic Structure Calculations on Workstation Computers: The Program System Turbomole. *Chem. Phys. Lett.* **1989**, *162*, 165−169.
(48) Brook, M.; Kaplan, J. Dissociation Energy of NO and N_2*. *Phys. Rev.* **1954**, *96*, 1540−1542.
(49) Bahn, S. R.; Jacobsen, K. W. An Object-Oriented Scripting Interface to a Legacy Electronic Structure Code. *Comput. Sci. Eng.* **2002**, *4*, 56−66.
(50) Perdew, J. Density-Functional Approximation for the Correlation Energy of the Inhomogeneous Electron Gas. *Phys. Rev. B: Condens. Matter Mater. Phys.* **1986**, *33*, 8822−8824.
(51) Becke, A. D. Density-Fnnctional Exchange-Energy Approximation with Correct Asymptotic Behavior. *Phys. Rev. A: At., Mol., Opt. Phys.* **1988**, *38*, 3098−3100.
(52) Maeda, S.; Morokuma, K. Communications: A Systematic Method for Locating Transition Structures of A+B→X Type Reactions. *J. Chem. Phys.* **2010**, *132*, 241102.
(53) Maeda, S.; Morokuma, K. Finding Reaction Pathways of Type A + B → X: Toward Systematic Prediction of Reaction Mechanisms. *J. Chem. Theory Comput.* **2011**, *7*, 2335−2345.
(54) Maeda, S.; Harabuchi, Y.; Sumiya, Y.; Takagi, M.; Suzuki, K.; Hatanaka, M.; Osada, Y.; Taketsugu, T.; Morokuma, K.; Ohno, K. GRRM, See http://iqce.jp/grrm/index_e.shtml.
(55) Hagberg, A. A.; Schult, D. A.; Swart, P. J. Exploring Network Structure, Dynamics, and Function Using NetworkX. In *Proceedings of the 7th Python in Science Conference*; Varoquaux, G., Vaught, T., Millman, J., Eds.; SciPy Conference: Pasadena, CA, 2008; pp 11−15.
(56) Tibshirani, R. Regression Shrinkage and Selection via the Lasso. *J. R. Stat. Soc. Ser. B* **1996**, *58*, 267−288.
(57) Fan, J.; Li, R. Variable Selection via Nonconcave Penalized Likelihood and Its Oracle Properties. *J. Am. Stat. Assoc.* **2001**, *96*, 1348−1360.
(58) Zhang, C. H. Nearly Unbiased Variable Selection under Minimax Concave Penalty. *Ann. Stat.* **2010**, *38*, 894−942.
(59) Breheny, P.; Huang, J. Coordinate Descent Algorithms for Nonconvex Penalized Regression, with Applications to Biological Feature Selection. *Ann. Appl. Stat.* **2011**, *5*, 232−253.
(60) Kasai, H.; Padama, A. A. B.; Nishihata, Y.; Tanaka, H.; Mitachi, C. Elements Science and Technology Project: Design of Precious Metal Free Catalyst for NO Dissociation. *J. Jpn. Pet. Inst.* **2013**, *56*, 357−365.
(61) Deushi, F.; Ishikawa, A.; Nakai, H. Density Functional Theory Analysis of Elementary Reactions in NOxReduction on Rh Surfaces and Rh Clusters. *J. Phys. Chem. C* **2017**, *121*, 15272−15281.
(62) Olson, J. A.; Garrison, B. J. Theory of Nonadiabatic Gas-Surface Reactions. *J. Chem. Phys.* **1985**, *83*, 1392−1403.
(63) Yasuike, T.; Nobusada, K. Quasi-Diabatic Decoupling of Born-Oppenheimer Potential Energy Curves for Adsorbate-Metal Surface Systems. *Chem. Phys. Lett.* **2008**, *457*, 241−245.
(64) Alducin, M.; Díez Muiño, R.; Juaristi, J. I. Non-Adiabatic Effects in Elementary Reaction Processes at Metal Surfaces. *Prog. Surf. Sci.* **2017**, *92*, 317−340.

DOI: 10.1021/acs.jpca.8b08868
J. Phys. Chem. A 2019, 123, 210−217